Available online at www.sciencedirect.com

ScienceDirect

Geochimica et Cosmochimica Acta 159 (2015) 112–125

Geochimica et Cosmochimica Acta

www.elsevier.com/locate/gca

Determining noble gas partitioning within a CO_2–H_2O system at elevated temperatures and pressures

Oliver Warr [a,b,*], Christopher A. Rochelle [c], Andrew Masters [d], Christopher J. Ballentine [a,b]

[a] School of Earth, Atmospheric and Environmental Sciences, Williamson Building, University of Manchester, Manchester M13 9PL, United Kingdom

[b] Department of Earth Sciences, University of Oxford, South Parks Road, Oxford OX1 3AN, United Kingdom

[c] British Geological Survey, Environmental Science Centre, Nicker Hill, Keyworth, Nottingham NG12 5GG, United Kingdom

[d] School of Chemical Engineering and Analytical Science, University of Manchester, Manchester M13 9PL, United Kingdom

Received 14 October 2014; accepted in revised form 2 March 2015; available online 11 March 2015

Abstract

Quantifying the distribution of noble gases between phases is essential for using these inert trace gases to track the processes controlling multi-phase subsurface systems. Here we present experimental data that defines noble gas partitioning for two phase CO_2–water systems. These are at the pressure and temperature range relevant for engineered systems used for anthropogenic carbon capture and geological storage (CCS) technologies, and CO_2-rich natural gas reservoirs (CO_2 density range 169–656 kg/m^3 at 323–377 K and 89–134 bar). The new partitioning data are compared to predictions of noble gas partitioning determined in low-pressure, pure noble gas–water systems for all noble gases except neon and radon. At low CO_2 density there was no difference between measured noble gas partitioning and that predicted in pure noble gas–water systems. At high CO_2 density, however, partition coefficients express significant deviation from pure noble gas–water systems. At 656 kg/m^3, these deviations are −35%, 74%, 113% and 319% for helium, argon, krypton and xenon, respectively. A second order polynomial fit to the data for each noble gas describes the deviation from the pure noble gas–water system as a function of CO_2 density. We argue that the difference between pure noble gas–water systems and the high density CO_2–water system is due to an enhanced degree of molecular interactions occurring within the dense CO_2 phase due to the combined effect of inductive and dispersive forces acting on the noble gases. As the magnitude of these forces are related to the size and polarisability of each noble gas, xenon followed by krypton and argon become significantly more soluble within dense CO_2. In the case of helium repulsive forces dominate and so it becomes less soluble as a function of CO_2 density.

1. INTRODUCTION

Noble gases are used as geochemical tracers to investigate a wide range of key geological systems (Porcelli et al., 2002; Burnard, 2013). Their inert natures prevent these noble gas tracers from chemically interacting with their surroundings. Thus their distribution within a geological system is a result of physical interaction between solids and different fluid phases. Consequently they can be used to interpret the physical processes which are often poorly constrained by other, more reactive, tracers. For example noble gases have proven their potential in topics as diverse as understanding the source, migration and sinks of fluids throughout the crust (e.g., Ballentine et al., 2002;

* Corresponding author at: Department of Earth Sciences, University of Oxford, South Parks Road, Oxford OX1 3AN, United Kingdom. Tel.: +44 1865 272000.

E-mail address: oliver.warr@earth.ox.ac.uk (O. Warr).

http://dx.doi.org/10.1016/j.gca.2015.03.003

0016-7037/

Sherwood-Lollar and Ballentine, 2009; Brennwald et al., 2013; Pinti et al., 2013) through to aiding our understanding of the origin and evolution of our planet (e.g., Holland et al., 2009; Marty, 2012; Halliday, 2013).

Noble gas utility is intrinsically linked to an understanding of their physical chemistry within the geological systems of interest. For systems where noble gas partitioning is undefined, estimations are typically made by approximating to experimentally determined low pressure systems which tend towards ideal gas behaviour. Although this approach provides a viable short term resolution, this creates uncertainties which restrict the usefulness of quantitative interpretations. The supercritical CO_2–water binary phase system in geological systems is a prime example as this can occur naturally (e.g., Ballentine et al., 2001; Ballentine and Holland, 2008) or anthropogenically for Enhanced Oil Recovery (EOR) (e.g., Blunt et al., 1993; Ravagnani et al., 2009). Additionally storage of anthropogenic CO_2 in geological structures as part of national CCS (Carbon Capture and Storage) strategies has further stimulated much recent interest in supercritical CO_2–water systems (Kharaka et al., 2006; Bickle et al., 2007; Cole et al., 2010). With this focus noble gases have been used extensively to understand the processes controlling CO_2 behaviour in the subsurface (Gilfillan et al., 2008, 2009; Dubacq et al., 2012; Zhou et al., 2012; Kampman et al., 2013) and they offer the potential to trace in-reservoir processes and subsurface leakage from engineered systems (Nimz and Hudson, 2005; Mackintosh and Ballentine, 2012).

Partitioning of noble gas i within a CO_2–water system is described using Henry's law:

$$\Phi_i P_i = \gamma_i K_i x_i \quad (1)$$

where P_i is the partial gas pressure of the noble gas, Φ_i is the fugacity, K_i is Henry's constant at a given temperature (T), x_i is the molar fraction of i within the liquid phase and γ_i is the activity coefficient. By combining system-specific fugacities and activity coefficients with the Henry's constant, Henry's coefficients (k_i) for noble gases at trace levels can be determined for the gas–liquid systems of interest:

$$k_i = \frac{\gamma_i K_i}{\Phi_i} \quad (2)$$

To date, water–CO_2 noble gas partitioning calculations within natural and engineered geological systems have been based on Henry's coefficients determined from noble gas–water experiments at low pressures (Crovetto et al., 1982; Smith and Kennedy, 1983; Smith, 1985) with the implicit assumption that a dense carbon dioxide phase will have no effect on noble gas fugacity. Additionally both the effect of aqueous CO_2 and pressure acting on the water phase are also assumed to have a negligible effect on the activity coefficient (Ballentine et al., 2002).

We assess here the effect of a dense CO_2 phase on Henry's coefficients by experimentally determining noble gas partitioning within high-pressure high-temperature supercritical carbon dioxide–water systems. These are compared with Henry's coefficients derived from the low pressure data sets (Crovetto et al., 1982; Smith, 1985). We discuss the physical causes for observed differences and we also provide a correlation that allows the calculation of Henry's coefficients for noble gases in the presence of carbon dioxide.

2. EXPERIMENTAL METHODS

2.1. Rationale

At optimal conditions for CCS storage, CO_2 densities typically range between 600 and 800 kg/m^3 (Bachu, 2003; IPCC, 2005; Friedmann, 2007). Where natural CO_2 systems are involved, assuming hydrostatic pressure, CO_2 densities range between 200 and 850 kg/m^3 (Bachu, 2003; Gilfillan et al., 2008). In this work a CO_2 density range between 169 and 656 kg/m^3 was selected to represent a wide variety of natural and anthropogenic crustal CO_2–water systems. This density range was achieved using a temperature and pressure grid which ranged between 323–377 K and 89–134 bar, respectively. The CO_2 density was thermodynamically derived via the NIST website (NIST, 2014). These are presented graphically on a CO_2 phase diagram (Fig. 1) and numerically (Table 1).

Binary phase CO_2–water systems, enriched with a noble gas spike, were created at the British Geological Survey (BGS) in Keyworth. Aliquots of each phase were subsequently sampled, sealed in pressurised containers, and transported to the School of Earth, Atmospheric and Environmental Sciences (SEAES), University of Manchester, where the respective noble gas components were isolated and their concentrations measured (Warr, 2013).

2.2. Sample generation

Samples were generated using a stainless steel pressurised batch reactor (Fig. 2). The reactor itself is initially

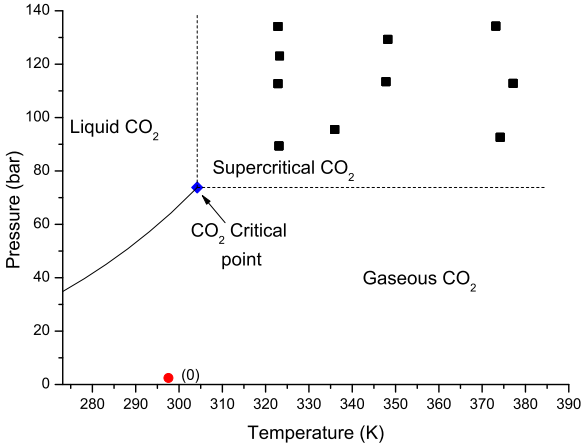

Fig. 1. Figure plotting the pressure and temperature of the experimental charges in this study and displayed in the context of the CO_2 phase diagram. All experimental data points were collected within the supercritical regime and are given in Table 1. Low pressure verification data point within gaseous CO_2 phase (Experiment 0) has also been included for reference.

Table 1
Thermodynamic conditions for all experiments displayed graphically in Fig. 1. The density of the CO_2 phase was calculated using the on-line calculator on the NIST website (NIST, 2014).

Experiment	Temperature (K)	Pressure (bar)	CO_2 density (kg/m^3)
0	298	2	4
1	323	89	281
2	323	113	535
3	323	123	602
4	323	134	656
5	336	96	252
6	348	113	290
7	348	129	363
8	374	93	169
9	377	113	216
10	373	134	284

charged with 150 cm^3 of deionised water and a magnetic stirrer bead was added and the system placed within an oven.

Three 1/8" Swagelok tube connections allow CO_2 injection and sampling, and the remaining two to act as inlet/outlet ports for water phase cycling and sampling. The oven was heated to the experiment temperature and laboratory grade CO_2 used to displace the air within the batch reactor. The sampler valve was closed and the headspace pressurised to the experiment pressure using an ISCO 260D syringe pump. A 1.5 cm^3 noble gas spike at ~0.6 bar containing 32% helium, 32% neon, 17% argon, 11% krypton, and 8% xenon was added to the headspace. After initial pressurisation the system was isolated from the CO_2 pump and the magnetic stirrer was turned on. An external Jasco PU-2086 HPLC pump circulated the water phase through the water samplers at 1 cm^3/min. After 24 hours, to compensate for CO_2 dissolution and thermal equilibration, additional CO_2 was added to regain target system pressure. The system was left to equilibrate for at least 14 days with a pump flow rate of 0.1 cm^3/min. During this time the pressure of the system was logged to ensure the system had no significant loss of CO_2. This was used as an indication that a closed system had been attained. Samples of the CO_2 and water phases were collected in triplicate.

Prior to sampling, experimental temperatures and pressures were recorded from a calibrated platinum-resistance thermometer connected to an Isotech calibration unit temperature probe and an ESI Technology transducer that had been checked against a second, externally-calibrated pressure transducer. For the water and CO_2 3 × 1.5 cm^3 and 3 × 1 cm^3 aliquots were sampled respectively using 1/8" stainless steel tubing with SS-ORS2 Swagelok needle valves at each end. An additional set of SS-ORS2 valves were attached to the CO_2 samplers as additional security against sample loss/contamination.

To sample the water phase the magnetic stirrer and HPLC pump were stopped and the valves on the water samplers were closed sequentially in order of proximity to the pump, starting with the closest. For the CO_2 phase

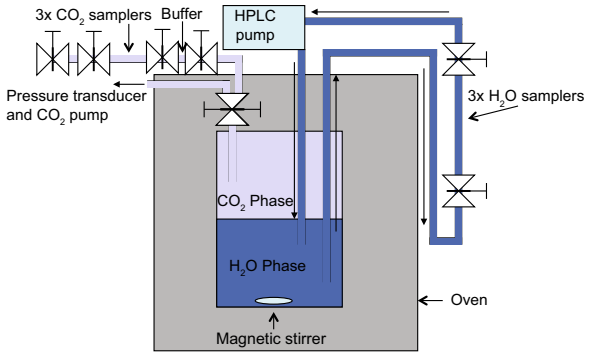

Fig. 2. Schematic of experimental equipment. A 200 cm^3 high pressure two-phase stainless steel batch reactor, rated to 500 bar, was placed within an oven and filled with 150 cm^3 of deionised water and 50 cm^3 of pressurised CO_2 containing a noble gas spike. A magnetic stirrer and HPLC pump were used to aid equilibration and ensure efficient mixing of the water phase. Samples were collected in triplicate using 1/8" diameter stainless steel tubing with Swagelok SS-ORS2 needle valves connected in series. For simplicity only one sampler for each phase is depicted here.

the samplers, initially filled with air at atmospheric pressure, were connected in series with all valves closed to the batch reactor at the CO_2 inlet/outlet valve (Fig. 2). To displace the air in the samplers ~120 cm^3 of CO_2 at atmospheric pressure and laboratory temperature (19 °C) (i.e., ~20× the total sampler and buffer volumes) was vented through the final sampler. All valves were then closed in order of furthest to nearest from the oven and the samplers removed. Due to the pressures involved and sampling at room temperature the CO_2 was sampled as a liquid phase. As noble gases exist in uniform trace amounts within the CO_2 phase the ratio of noble gas to CO_2 is independent to the phase of collection within a closed system.

2.3. Sample analysis

CO_2 and water phase samples were each prepared and analysed in an all metal UHV system using a Hiden Analytical 1–200 AMU (HAL200) quadrupole mass spectrometer (Fig. 3). Through a process of expansions, dilutions and chemical reactions the noble gas component was isolated prior to measurement (Warr, 2013).

All samples were connected to the analytical line using 1/8" stainless steel Swagelok fittings (Fig. 3). After standard operating pressures were reached in the quadrupole volume (6×10^{-11} bar) the CO_2 sample buffer volume was evacuated using the roughing pump. The buffer valve was closed and the system was again pumped down to reach operating pressure. To check for leakage on mounting each sample the pressure was monitored by opening to the closed volume containing the 0–13.33 bar Baratron® after reopening the buffer volume. Negligible deflection on the Baratron® for all samples indicated a contribution of <0.03% to all measured noble gases due to leakage from the sample connection, with full procedural blanks confirming negligible noble gas contributions from sources other than the sample aliquots.

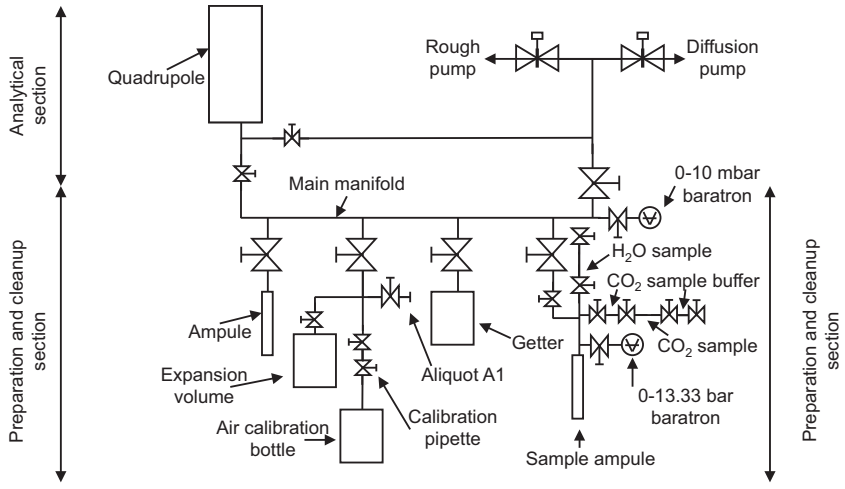

Fig. 3. Schematic of the noble gas analysis line used to determine noble gas concentrations of each phase. The line is broadly split into two sections; a preparation and cleanup section where samples are expanded, aliquoted and cleaned, and an analytical section where the noble gas content is quantitatively determined using the quadrupole.

The CO_2 sample was expanded to the cleanup section and left to equilibrate for 2 min. Aliquot A1 (0.81 cm^3) was used to reduce the volume of CO_2 and the remainder of the vacuum line opened to the pump until operating pressures were once again reached. The CO_2 aliquot was exposed to a hot SAES NP10 getter for 10 min to remove all active gases via chemical reaction before being expanded to the quadrupole analyser for noble gas determination. The noble gas isotopes measured are listed in Table 2.

The noble gas content of each sample was measured for 10 min after which the sample was pumped away. In addition, a baseline reading for each isotope was collected for 10 min before and after sample analysis.

Water sample preparation involved a two stage cryogenic approach to remove the water phase. The water sample was released into the underlying stainless steel sample receptacle where it was degassed using an ultrasonic bath to ensure that the helium and neon occupied the headspace. The receptacle containing the water was then cooled with liquid nitrogen leaving helium and neon and >5% of argon in the headspace. The headspace was expanded into the clean-up section and the Ampule aliquot (Fig. 3) was used to reduce the volume by a factor of 0.014. The clean-up section was then pumped to standard operating pressures after which the Ampule aliquot was reopened to the cleanup section and exposed to the hot SAES NP10 getter prior to analysis.

Argon, krypton and xenon were released into the headspace by warming the sample receptacle to room temperature followed by ultrasonic degassing. The sample receptacle was then immersed in an acetone slush (178 K) to re-freeze the water. The heavy noble gases, now in the headspace, followed an identical procedure as described for helium and neon. Post-degassing redissolution resulted in a maximum, negligible (<0.2%) reduction in headspace values.

Table 2
Noble gas isotopes measured to derive Henry's coefficients during sample analysis of each sample. Neon results not used (see text).

Noble gas	Isotope(s)
Helium	^{4}He
Neon	^{20}Ne, ^{21}Ne, ^{22}Ne
Argon	^{40}Ar
Krypton	^{82}Kr, ^{84}Kr
Xenon	^{132}Xe, ^{136}Xe

2.4. Data analysis

System stability and linearity are provided in Appendix 2. Initial raw signal intensities for each isotope were determined for the CO_2 and water phases ($C_{i(\mathrm{raw})}$ and $W_{i(\mathrm{raw})}$, respectively). A baseline measurement ($C_{i(\mathrm{back})}$ and $W_{i(\mathrm{back})}$) was also measured which was then subtracted from these raw signal intensities. Procedural blanks indicated no discernible background above baseline values and therefore the baseline correction alone was applied. Next, a series of corrections were applied to negate measured differences in both sample and analytical aliquot sizes, as well as increases to sample density due to sampling both experimental phases at room temperature. Consequently signals were standardised for each noble gas isotope (i) for the CO_2 and water phases for the experimental pressures (P) and temperatures (T) ($C_{i(P,T)}$ and $W_{i(P,T)}$, respectively). These corrected, dimensionless, noble gas peak intensities of each phase were then used to generate a phase ratio for each noble gas isotope:

$$D_{i(P,T)} = \frac{C_{i(P,T)}}{W_{i(P,T)}} \quad (3)$$

where $D_{i(P,T)}$ is the dimensionless partitioning ratio of noble gas isotope i between each phase at a given pressure (P) and temperature (T).

The partitioning ratios were determined three times in each experiment. An arithmetic mean of these three data points was used to generate partitioning ratios for each isotope. Through comparison with predicted partitioning based on pure noble gas–water Henry's coefficients (Crovetto et al., 1982; Smith, 1985) Henry's coefficients were obtained (see Table 4). The method for deriving the uncertainty associated with each data point is provided in Appendix 1.

2.5. Experimental verification

In order to verify the experimental procedure, experiments were conducted at ambient temperature and pressure (Experiment 0, Table 1). Under these conditions Henry's coefficients in a CO_2–water system are expected to be indistinguishable from pure noble gas–water values.

Ambient pressure and temperature results are presented in Table 3. For both argon and krypton the pure noble gas–water values were experimentally reproduced within 1σ uncertainty. Although xenon partitioning was slightly over-predicted the pure noble gas–water values are within 2σ (95% confidence) of the experimental values. Uncertainty in the helium determination was significantly higher due to the low solubility of helium in water resulting in a yet smaller signal size. Helium partitioning values are nevertheless within 2σ of predicted values. Low signal size was a concern and these experiments resulted in an increase in the amount of noble gas being added into the system during initial pressurisation of the system (see Section 2.2) to ensure helium was present in greater abundances resulting in lower, acceptable, uncertainties (see Table 6).

3. RESULTS

The experimentally measured Henry's coefficients for each noble gas are given in Table 4. All values are presented here as deviation from pure noble gas water Henry's coefficients as well as absolute values. The pure noble gas–water values are reproduced in Table 5 and experimental deviation from predicted values are given in Table 6.

3.1. Quantifying density-deviation trends

Physical properties of CO_2 such as density, enthalpy and viscosity do not deviate from their current trends when migrating across the supercritical–subcritical "boundary" (Span and Wagner, 1996; NIST, 2014). It is reasonable to assume noble gas trends are similarly unaffected across the supercritical and subcritical CO_2 transition. As such, any deviations in noble gas partitioning behaviour from low pressure behaviour are reasonably controlled by increased molecular interactions and related to density. Indeed, for all noble gases, deviations from pure noble gas–water systems as a function of CO_2 density are observed. This deviation trend is negative for helium and positive for argon, krypton and xenon (Table 6, Fig. 4).

Table 3
Comparing experimental Henry's coefficients with their pure noble gas–water counterparts under ambient conditions. All Henry's coefficients are given in GPa to 2 decimal places. Ratios were derived from ^{4}He, ^{40}Ar, ^{82}Kr, ^{84}Kr, ^{132}Xe & ^{136}Xe. For reasons outlined in Section 3.5 Henry's coefficients for neon could not be determined. Noble gas–water values are taken from Crovetto et al. (1982) and Smith (1985). Uncertainties for noble gas–water values are calculated using values in Table 7 with Eq. (4). All uncertainty is given as 1σ confidence.

Noble gas	Noble gas–water Henry's coefficient (GPa)	Experimental Henry's coefficient (GPa)
Helium	14.59 ± 1.38	8.28 ± 4.81
Argon	4.02 ± 0.49	3.77 ± 0.59
Krypton	2.22 ± 0.21	2.14 ± 0.22
Xenon	1.31 ± 0.21	1.89 ± 0.23

Table 4
Experimentally derived Henry's coefficients for all noble gases. Values are given in GPa and are quoted to 2 decimal places. Uncertainty is given as 1σ confidence. *Indicates no viable partition coefficient was generated.

Experiment	Helium (GPa)	Neon (GPa)	Argon (GPa)	Krypton (GPa)	Xenon (GPa)
0	8.28 ± 4.81	*	3.77 ± 0.59	2.14 ± 0.22	1.89 ± 0.23
1	13.2 ± 2.35	18.82 ± 6.91	6.02 ± 0.87	4.16 ± 0.38	3.69 ± 0.23
2	11.39 ± 2.01	23.48 ± 28.5	8.07 ± 1.18	7.23 ± 0.68	8.44 ± 0.64
3	13.55 ± 2.38	19.49 ± 17.66	4.58 ± 0.72	6.06 ± 0.6	7.90 ± 1.04
4	6.73 ± 1.19	16.42 ± 20.98	9.81 ± 1.43	6.93 ± 0.65	8.64 ± 0.68
5	13.76 ± 2.44	22.77 ± 8.13	8.46 ± 1.26	5.17 ± 0.47	4.19 ± 0.26
6	10.19 ± 1.81	19.47 ± 22.69	6.46 ± 0.96	5.01 ± 0.46	5.42 ± 0.4
7	13.05 ± 2.29	22.06 ± 10.25	6.94 ± 1.08	5.86 ± 0.53	6.76 ± 0.43
8	9.64 ± 1.71	8.28 ± 5.69	7.96 ± 1.27	5.27 ± 0.48	4.92 ± 0.35
9	12.08 ± 2.13	22.02 ± 17.07	5.50 ± 0.83	5.27 ± 0.49	4.92 ± 0.32
10	12.72 ± 2.24	22.61 ± 13.86	5.98 ± 0.93	5.47 ± 0.51	5.76 ± 0.38

Table 5
Pure noble gas–water Henry's coefficients for all noble gases. Helium values taken from Smith (1985) and neon, argon, krypton and xenon values taken from Crovetto et al. (1982). Values are given in GPa and are quoted to 2 decimal places.

Experiment	Helium (GPa)	Neon (GPa)	Argon (GPa)	Krypton (GPa)	Xenon (GPa)
0	14.59	12.48	4.02	2.22	1.31
1	14.50	13.49	5.57	3.36	2.21
2	14.50	13.49	5.56	3.35	2.21
3	14.49	13.50	5.58	3.37	2.22
4	14.50	13.49	5.56	3.35	2.21
5	13.92	13.43	6.09	3.80	2.59
6	13.19	13.10	6.39	4.11	2.86
7	13.16	13.09	6.39	4.12	2.87
8	11.18	11.79	6.49	4.43	3.18
9	10.93	11.61	6.46	4.44	3.19
10	11.26	11.85	6.49	4.43	3.17

Table 6
Experimental Henry's coefficients displayed as percentage deviations from values calculated for a pure noble gas water system (Table 5). Negative values indicate lower Henry's coefficients than predicted i.e., a greater solubility within the water phase (Eq. 1) and vice versa. All values are given to 2 decimal places. *Indicates no viable partition coefficient was generated.

Exp.	Helium (%)	Neon (%)	Argon (%)	Krypton (%)	Xenon (%)
0	-43.24 ± 58.11	*	-6.24 ± 15.77	-3.97 ± 10.15	44.48 ± 11.97
1	-8.98 ± 17.79	39.46 ± 36.74	8.15 ± 14.52	23.93 ± 9.06	66.83 ± 6.20
2	-21.48 ± 17.68	74.04 ± 121.37	45.14 ± 14.66	115.87 ± 9.33	282.36 ± 7.59
3	-6.48 ± 17.55	44.44 ± 90.60	-17.77 ± 15.71	80.19 ± 9.81	255.91 ± 13.20
4	-53.63 ± 17.65	21.71 ± 127.72	76.51 ± 14.56	106.84 ± 9.41	291.60 ± 7.83
5	-1.18 ± 17.76	69.57 ± 35.71	39.00 ± 14.83	36.01 ± 9.12	61.65 ± 6.29
6	-22.76 ± 17.74	48.59 ± 116.53	1.24 ± 14.88	21.87 ± 9.24	89.39 ± 7.42
7	-0.83 ± 17.57	68.59 ± 46.46	8.53 ± 15.61	42.40 ± 9.12	135.56 ± 6.40
8	-13.72 ± 17.70	-29.76 ± 68.70	22.76 ± 15.91	18.83 ± 9.17	54.79 ± 7.15
9	10.52 ± 17.61	89.73 ± 77.54	-14.87 ± 15.06	18.71 ± 9.21	53.91 ± 6.44
10	12.96 ± 17.61	90.85 ± 61.31	-7.87 ± 15.55	23.52 ± 9.37	81.35 ± 6.55

Without a detailed mechanistic understanding of the role of CO_2 density in determining the noble gas data any fit of the data to a function cannot be used to extrapolate the data beyond the physical conditions of these experiments. Nevertheless, such a fit provides a pragmatic tool for correcting noble gas partition data over the range of densities covered by this work.

At very low densities ideal gas behaviour can reasonably be assumed, and is demonstrated during our experimental validation. Consequently a full reconciliation is expected with pure noble gas–water systems where as density $\rightarrow 0$; deviation from pure noble gas–water values $\rightarrow 0$. For each of the noble gases an error weighted second-order polynomial fit line which passes through the origin is has been determined for the form:

$$y = ax^2 + bx + c \tag{4}$$

where x is the density, a, b and c are coefficients (with c fixed at 0) and y is percentage deviation. We also determined the $\pm 1\sigma$ confidence envelope for each of the polynomial fits with associated a, b and c coefficients. Accordingly a single equation is provided which characterises the deviation in Henry's coefficient from a low pressure water–gas system for each noble gas for the 0–656 kg/m^3 CO_2 density range (Table 7).

The polynomial fit can be very simply used to directly derive the deviation coefficient from a low pressure water–gas system by applying the equation:

$$\kappa_i = \frac{(a_i x^2 + b_i x + c_i)}{100} + 1 \tag{5}$$

where a, b and c are the fitted coefficients for noble gas i (Table 7), x is the CO_2 density in kg/m^3 and $a_i x^2 + b_i x + c$ gives the percentage deviation from pure noble gas–water values. Using this deviation coefficient, Henry's coefficients for a pure noble gas–water system ($k_{i(\mathrm{pub})}$), taken from Crovetto et al. (1982) and Smith (1985), can be recalculated for application to dense CO_2-rich systems ($k_{i(CO_2)}$):

$$k_{i(CO_2)} = \kappa_i k_{i(\mathrm{pub})} \tag{6}$$

3.2. Xenon

Experimental Henry's coefficients were all significantly larger than predicted with values increased by between 53.9% and 291.6%. From Fig. 4A, a clear, positive CO_2 density-deviation trend from pure noble gas–water partitioning was observed. A high R^2 (0.98) indicates that the polynomial can be used with reasonable confidence to predict the CO_2 density-deviation relationship within the

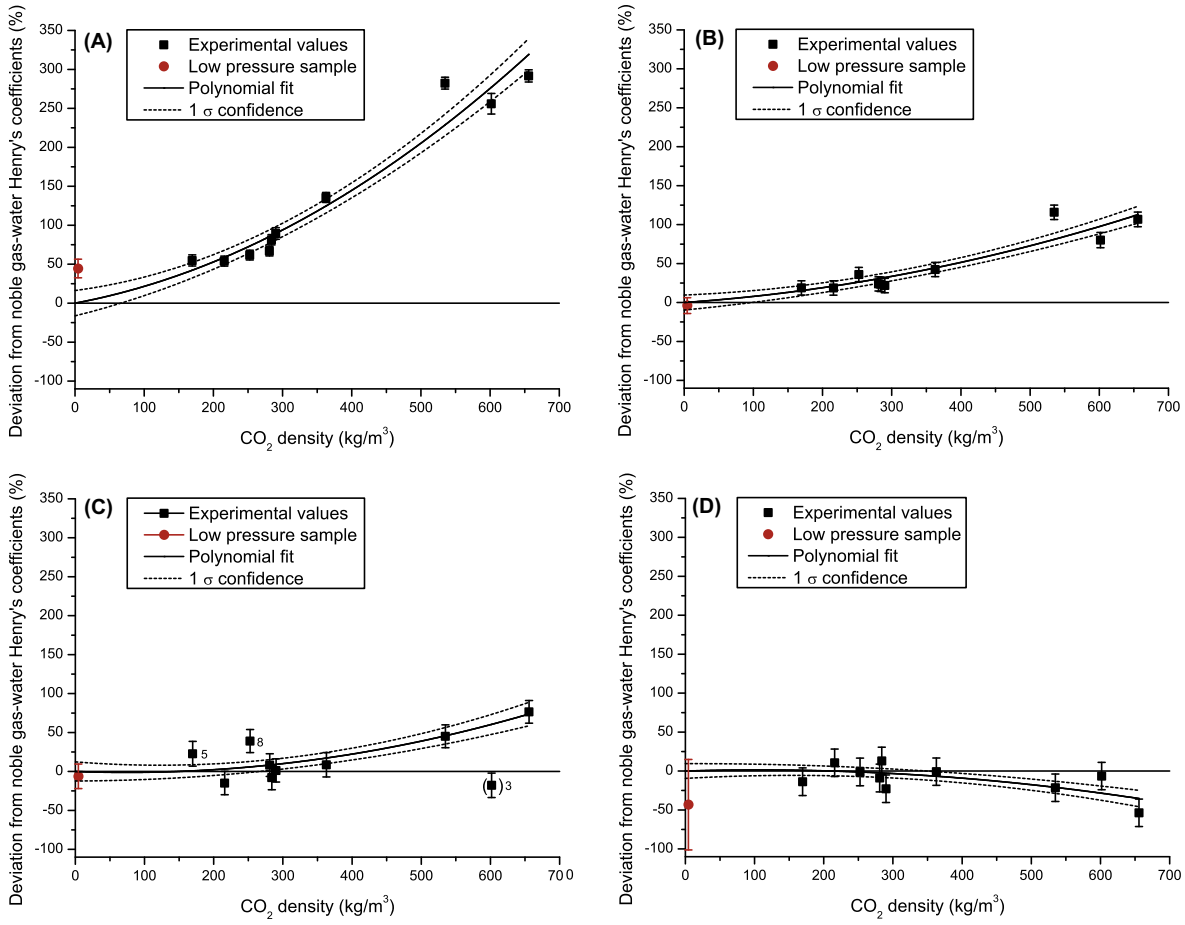

Fig. 4. Deviations of experimental Henry's coefficients for xenon (A), krypton (B), argon (C) and helium (D) from pure noble gas–water behaviour (Crovetto et al., 1982; Smith, 1985) as a function of CO_2 density. CO_2 density was calculated via the NIST website (NIST, 2014). Coefficients for each polynomial and their 1σ confidence envelopes are given in Table 7. Low pressure samples (Experiment 0) are provided for reference and discussed fully in Section 2.5.

experimental density range. Using this fit, Henry's coefficients reconcile with those for a pure noble gas–water system (⩽5% deviation) at CO_2 densities lower than 28 kg/m^3. This polynomial is considered to suitably define deviation from a pure noble gas–water system as a function of CO_2 density for the ~0–656 kg/m^3 range.

3.3. Krypton

All experimentally-defined Henry's coefficients exceed those predicted for pure noble gas–water systems, with deviations ranging from 18.7% to 115.9% at the highest density. By plotting deviation as a function of density a positive CO_2 density-deviation trend is again observed (Fig. 4B). When extrapolated to lower densities the polynomial predicts progressive reconciliation with pure noble gas–water values, with deviations less than 5% (i.e., within typical experimental uncertainty) at densities below 69 kg/m^3. Given the good fit to the experimental data ($R^2 = 0.94$) and the reconciliation with partitioning for noble gas–water systems at low densities, the polynomial fit provides a viable method of defining deviation from pure

Table 7
Coefficients to fit Eq. (4) for deriving deviation from pure noble gas–water partitioning as a function of CO_2 density between 0 and 656 kg/m^3. R^2 values are given to indicate confidence of polynomial fit to experimental values. Coefficients are also given for calculating 1σ uncertainty via Eq. (4). All values are given to three significant figures.

Noble Gas	Coefficient a	Coefficient b	Coefficient c	R^2
Helium	−1.213E−04	2.564E−02	0	0.48
$+1\sigma$	−8.195E−05	1.430E−03	9.467E+00	
-1σ	−1.607E−04	4.985E−02	−9.467E+00	
Argon	2.218E−04	−3.297E−02	0	0.73
$+1\sigma$	2.841E−04	−6.945E−02	1.226E+01	
-1σ	1.595E−04	3.510E−03	−1.226E+01	
Krypton	1.685E−04	6.142E−02	0	0.94
$+1\sigma$	2.099E−04	3.617E−02	9.680E+00	
-1σ	1.271E−04	8.667E−02	−9.680E+00	
Xenon	4.873E−04	1.671E−01	0	0.98
$+1\sigma$	5.771E−04	1.146E−01	1.626E+01	
-1σ	3.976E−04	2.195E−01	−1.626E+01	

noble gas–water systems as a function of CO_2 density for the 0–656 kg/m^3 range.

3.4. Argon

Most argon Henry's coefficients were close to or within pure noble gas–water values. However, at sufficiently high CO_2 densities, a general positive deviation emerges (Fig. 4C). At low density no overall deviation from the pure noble gas–water partition coefficients was observed. Experiments 5 and 8 (169 & 252 kg/m^3) showed high relative CO_2 phase concentrations. Argon is susceptible to air contamination and it is possible that some of the variance at both low and high CO_2 density may be due to trapped air in the sampling process. However, as they broadly supported the trends seen for argon and the heavier noble gases (i.e., positive deviation) Experiments 5 and 8 were included in the polynomial fit. In contrast, Experiment 3 (602 kg/m^3) did not fit the overall positive trend. Given that this otherwise positive density-deviation trend is strongly reinforced by both closest sister elements, krypton and xenon, the validity of this data point was doubtful and has been omitted from the polynomial fit. This resultant fit reached reasonable agreement with the data ($R^2 = 0.73$) and expressed deviations greater than 5% of pure noble gas–water values at 242 kg/m^3. This polynomial can therefore be used to predict deviation from pure noble gas–water systems as a function of CO_2 density for the 0–656 kg/m^3 range for argon.

3.5. Neon

^{20}Ne, ^{21}Ne, and ^{22}Ne were measured in both phases. However the quadrupole is unable to resolve contributions from doubly charged interference ions $^{40}Ar^{++}$, and CO_2^{++} contributing to masses 20 and 22, respectively. Although the relationship between singly and doubly charged ions for the Hiden Quadrupole Mass Spectrometer is constrained, these interferences are substantial and. the propagated error when correcting for doubly charged ions results in unresolvable Henry's coefficients for ^{20}Ne and ^{22}Ne. The remaining isotope, ^{21}Ne, is only present in minor quantities and the signal size from the water phase resulted in large uncertainties. While we report the Ne data for completeness (Tables 4–6), no conclusions are reached for neon behaviour within dense CO_2–water systems in this work and future experiments will need either a larger relative Ne spike or to adopt analytical instruments with the ability to resolve or accurately correct for the interference peaks. This issue is specific to neon and therefore all other noble gas Henry's coefficients remained unaffected.

3.6. Helium

At low density most experimental values are within uncertainty indistinguishable from pure noble gas/water values. Overall, a progressive negative deviation trend was observed as a function of increasing density, characterised by the second order polynomial with deviations greater than 5% of pure noble gas–water systems (i.e., exceeding experimental uncertainty) at CO_2 densities of 335 kg/m^3 (Fig. 4D). The polynomial fit allows correction for the CO_2 density-derived deviation from pure noble gas–water systems to be interpolated for a CO_2 density range of 0–656 kg/m^3.

4. DISCUSSION

From Eq. (2), Henry's coefficients for noble gases in both CO_2–water and noble gas water systems are the net effect of non-ideality in both phases acting on the Henry's constant. Differences between the two Henry's coefficients therefore are due to changes in these non-ideal terms which require evaluation.

4.1. Non-ideality in the water phase

The temperature range presented here fell within the original pure noble gas–water range (Crovetto et al., 1982; Smith, 1985). Therefore thermal controls on solubility within the water phase were already accounted for. At pressures relevant to the experiment designed here, pressure can have an effect on Henry's coefficients (Hou et al., 2013) and can be quantified using the Poynting correction (Enns et al., 1965; Prini and Crovetto, 1989).

$$\Phi_i P_i = \gamma_i K^0_{i_i} x_i e^{\left(\frac{\overline{V}_{mi}(P-P^0)}{RT}\right)} \quad (7)$$

where $\overline{V}_{mi}$ is the partial molar volume of i at infinite dilution at reference pressure P^0, P is the experimental pressure, $K^0_{i_i}$ is Henry's constant at the reference pressure, R is the ideal gas constant and T is the temperature. Partial molar volume is considered pressure independent (Enns et al., 1965; Gerth, 1983; Prini and Crovetto, 1989; Poling et al., 2001). Values of $\overline{V}_{mi}$, for each noble gas are given in Table 8.

The Poynting correction was applied to the experimental conditions which yielded the highest density (Experiment 4, 656 kg/m^3) to determine the maximum effect pressure-derived non-ideality in the water phase has on Henry's coefficients (Table 9).

From Table 9 although pressure has a minor effect on solubility the majority of the observed deviations remain unaccounted for. Additionally for helium, contrary to the observed trend, the Poynting correction indicates a lower solubility as a function of increasing pressure. Both observations are indicative that pressure acting on the

Table 8
Partial molar volumes of each noble gas at infinite dilution. Helium and argon values taken from Enns et al. (1965), krypton value taken from Moore et al. (1982) and xenon value taken from Biggerstaff and Wood (1988).

Noble gas	Partial molar volume (cm^3/mol)
Helium	29.7
Argon	32.2
Krypton	32.8
Xenon	42.7

Table 9
Assessing the effects of the Poynting correction on Henry's coefficients for the highest experimental density (656 kg/m^3) where deviations were at their greatest. Partial molar volumes for each noble gas are taken from Table 8. The outstanding deviations are the deviations derived using Eq. (4) minus those which can be attributed to pressure effects.

Noble gas	Change to partitioning due to pressure (%)	Experimental deviation (%)	Outstanding deviation (%)
Helium	16	−35	−51
Argon	17	74	57
Krypton	18	113	95
Xenon	24	319	295

water phase has a relatively minor effect. Consequently this is discounted as the driving force affecting partitioning.

Currently the effect of $CO_{2(aq)}$ on noble gas solubility remains unquantified (Ballentine et al., 2002). However, it is reasonable to assume that $CO_{2(aq)}$ will reduce noble gas solubility given the finite capacity of water for non-polar solute particles at fixed P,T conditions. Experimental $CO_{2(aq)}$ concentrations range between 0.73 and 1.13 mol/l (Spycher et al., 2003). Under these concentrations the $CO_{2(aq)}$ activity coefficient remains at unity (Diamond and Akinfiev, 2003) therefore no significant change in overall behaviour or internal structure of the water phase can be assumed. Accordingly, a negligible effect on the chemical potential of a dissolved inert gas is expected.

Neither pressure nor $CO_{2(aq)}$ adequately account for the observed deviations from pure noble gas–water Henry's coefficients. With no additional factors attributable to water phase non-ideality, non-ideality in the water phase can be ruled out as the dominant force driving the observed deviations in Henry's coefficients.

4.2. Non-ideality in the CO_2 phase

At sufficiently high densities a departure from the ideal gas law due to enhanced molecular interactions within the CO_2 phase is expected. CO_2–noble gas interactions are similarly expected to become significant at higher densities. With all water phase factors discounted it is these enhanced interactions that are expected to be the source of deviation. For argon, krypton and xenon this non-ideality is expressed as a greater affinity for the CO_2 phase ($\Phi_i < 1$), while with helium the opposite is observed ($\Phi_i > 1$).

Presently the effect of water within the CO_2 phase on Henry's coefficients is undocumented. However, under the conditions where deviations are at their greatest (Experiment 4) the molar fraction of water within the CO_2 phase is extremely low (0.006, Briones et al., 1987). Additionally, for any given pressure, the molar fraction of water increases with temperature (Spycher et al., 2003); this corresponds with decreasing CO_2 density and therefore does not fit with the observed trends. Consequently it is reasonable to assume water within this phase has a negligible effect on partitioning.

Dense CO_2 acts as a fluid solvent (e.g., Kamihira et al., 1987; Black, 1996; Morgenstern et al., 1996). This allows application within a wide range of industrial processes such as decaffeination (e.g., Mohamed et al., 2002; Kim et al., 2008), Enhanced Oil Recovery (EOR) (e.g., Blunt et al., 1993; Ravagnani et al., 2009) or in pharmaceutical processes (e.g., Ferrieri, 2003; Reverchon et al., 2009). As the solvation power of a fluid increases as a function of density (Giddings et al., 1968; Yonker et al., 1986) a link between CO_2 density (i.e., non-ideality) and solvation power can be assumed (Baiker, 1999). In addition there will be dispersion effects, related to atomic size, which also increase as a function of density. Coupled with this, dense CO_2 phases possess polar properties (e.g., Reynolds et al., 1996; Kauffman, 2001; Raveendran et al., 2005). Therefore, noble gas solubility within the CO_2 phase is expected to be enhanced in order of both molecular size and polarisability (i.e., xenon → helium). Similar induced polarisation solubility trends are observed within the water phase (Ballentine et al., 2002; Kipfer et al., 2002). Helium solubility however is reduced as a function of CO_2 density. This is considered to be due to the low polarisability of helium resulting in the net repulsive forces in the CO_2 phase at higher density outweighing the enhanced attractive forces. The positive fugacity is already observed in the pure noble gas phase at low temperature high pressure (Ballentine et al., 2002, Table 1). Thus helium behaviour is also satisfactorily described via this mechanism.

4.3. Extrapolating observed deviation trends?

Overall, deviations increased as a function of density for all noble gases and this trend in the data is well-defined using a second order polynomial. To extrapolate these polynomials beyond the range presented here would presume that the forces driving deviation continue to respond accordingly to changes in CO_2 density. Additionally the assumption that no other factor will significantly affect noble gas partitioning would have to be maintained, regardless of changes to the thermodynamic conditions outlined in this work. At present no data supports either assumption. Consequently the experimentally defined trend lines cannot reasonably be extrapolated beyond the range presented.

4.4. Impacts of study on geological processes

Noble gas phase partitioning within dense CO_2 environments deviates strongly from low-density predictions. Consequently, where low pressure partitioning has been assumed, a moderate degree of recalculation will be required to maintain mass-balance as in the case study example. For example processes which increase the noble gas content of a CO_2 phase (e.g., degassing of groundwater) will require scaling down. Additionally key isotopic ratios such as $^4He/^{40}Ar$, $^{84}Kr/^{36}Ar$ will also be affected. The CO_2 density must therefore be considered where such ratios are used to quantify geological processes. Similarly, due to this change in relative Henry's coefficients, a re-evaluation

of all models involving open Rayleigh degassing in CO_2 environments is required.

The Henry's coefficients presented here can be used to re-interpret previous, related studies. As an example we consider the paper of Gilfillan et al. (2008) which uses noble gases to consider the processes controlling CO_2 emplacement and removal in naturally occurring CO_2 in the Sheep Mountain and Bravo Dome gas fields (Colorado and New Mexico, USA). Here we re-evaluate the models employed in order to take into account the effect of dense CO_2. For a full geological history and analytical methodology the reader is directed to the original text (Gilfillan et al., 2008). As a summary, Air-Saturated Water (ASW) noble gases are initially considered to be completely stripped out of the water phase due to sustained injection of magmatic CO_2. This results in a gas field that is dominated by CO_2 containing noble gases in ASW proportions. Following reservoir filling, a period of redissolution occurs. This redissolution was modelled as open system noble gas loss from the CO_2 phase. The fractionation of noble gases remaining within the CO_2 phase was modelled for both fields as Raleigh loss using Henry's coefficients. Graphs showing original and re-evaluated fractionation via redissolution curves for Bravo Dome and Sheep Mountain are presented in Fig. 5A and B.

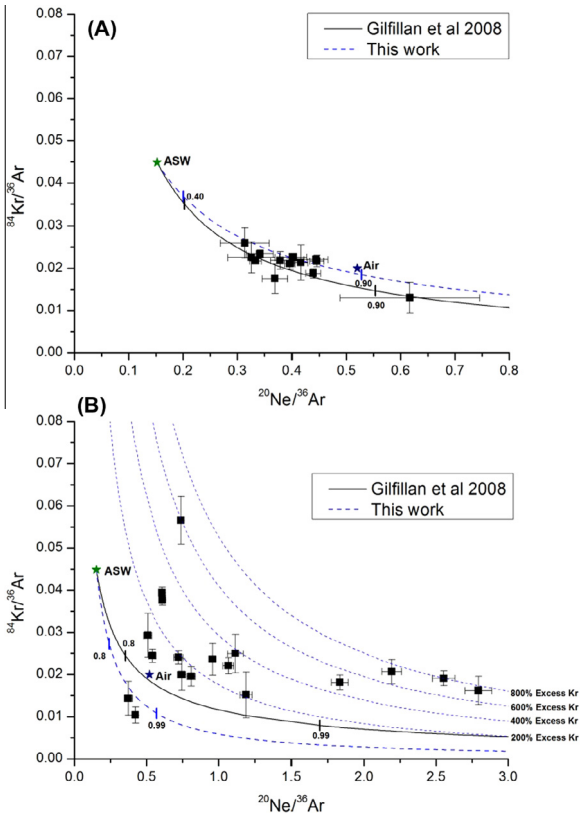

Fig. 5. Original and re-evaluated noble gas fractionation via redissolution curves for Bravo Dome (A) and Sheep Mountain (B). ASW indicates initial, Air Saturated Water values. The solid lines indicate redissolution proposed by Gilfillan et al. (2008) and the dashed lines are the re-evaluated dissolution curves using Henry's coefficients from this work. Tick lines indicate relative fraction of argon loss from gas phase.

For the Sheep Mountain gas field an additional initial krypton component 400% in excess of ASW values was proposed, in order to be consistent with the physical model. In the absence of Henry's coefficients for CO_2–water systems the effect of CO_2 was estimated using virial coefficients to calculate pressure-derived fugacities (Ballentine et al., 2002). For this case study the Henry's coefficients, calculated for reservoir temperatures and salinities, are recalculated to incorporate the CO_2-derived density deviations presented in this work. For neon values the virial-derived Gilfillan et al., values are used as these remain the best estimation of neon non-ideal behaviour (Fig. 5).

In the case of Bravo Dome, although a slightly shallower fractionation gradient is observed, the curve still reaches good agreement with the measured data (Fig. 5A). This indicates that after including the effect of dense CO_2 (273 kg/m^3) the straightforward redissolution model remains viable for Bravo Dome. However, in the case of Sheep Mountain, where CO_2 density was significantly higher (572 kg/m^3), a greater effect is observed (Fig. 5B). Where originally an excess of 400% initial krypton was required to reconcile the dissolution model with the data, the new, significantly steeper, fractionation gradient requires an initial excess of ~700%. This increased excess therefore requires a greater external input of krypton e.g. excess air or organic sediments.

4.5. Related systems

Re-evaluation is required of closely related binary systems. As the CO_2 density is responsible for the observed deviations, similar deviations should also be expected wherever a dense CO_2 phase is encountered. The CO_2-magma system is a prime example. During the ascent of magma, depressurisation results in the formation of separate phases (i.e., vesicles) within the melt (e.g., Paonita and Martelli, 2006, 2007). The vesicles consist of almost pure CO_2 (Carroll and Draper, 1994) which at those temperatures and pressures exists as a supercritical fluid (Sparks, 1978; NIST, 2014). The noble gases partition between the CO_2 and melt with a strong preference for the CO_2 phase. This partitioning is used to constrain variables such as degassing rates and magmatic origins. However, the partitioning coefficients used for this were derived from low pressure experiments and assume only melt composition affects noble gas partitioning (Jambon et al., 1986; Carroll and Draper, 1994; Hilton and Porcelli, 2003), and the effect of dense CO_2 is therefore considered negligible. Our study indicates the weakness in this assumption. Indeed recent simulation-based studies of CO_2-magma systems suggest that CO_2 density is an important model component (Sarda and Guillot, 2005; Guillot and Sarda, 2006; Aubry et al., 2013).

Our work indicates CO_2 density is liable to affect partitioning within all CO_2-based systems. These potentially include CO_2-hydrocarbon, CO_2-mantle and CO_2-hydrothermal fluid environments. It is therefore advised that wherever a dense CO_2 phase is present, noble

gas partitioning is liable to be poorly predicted by low pressure analogues.

Additionally, as differences are due to changes in the non-ideal terms derived for low densities, an argument can be made that noble gas behaviour within all dense binary phase geological systems, not just those involving CO_2, may require a degree of re-examination. A prime example is the methane–water system for which noble gases provide industrial and academic insights (e.g., Zhou et al., 2005; Hunt et al., 2012). However, noble gas behaviour within this system remains experimentally uncharacterised. Traditionally pure noble gas–water partitioning would be considered comparable for this system, but our work highlights the issue in making such an assumption. Accordingly, independent experimental investigation of noble gas behaviour is required.

5. SUMMARY

Noble gas Henry's coefficients for supercritical CO_2–water systems do not replicate pure noble gas–water system values. This is due to density-derived non-ideality within the CO_2 phase. As density increases so too do deviations from predicted partition coefficients for all noble gases. These deviations are positive for argon, krypton and xenon. Helium possesses a negative deviation as a function of density and consequently decreases as a function of density. Deviations are most likely caused by dispersion effects related to atomic size coupled with CO_2 acting as a polar solvent with the solvation power increasing as a function of density. Polarisation is induced in each noble gas in line with their respective polarisabilities. Xenon affinity for the dense CO_2 phase is increased the most followed by krypton and then argon. This therefore results in positive deviations to the pure noble gas–water partition coefficients. Helium being far less polarisable and having the smallest atomic size has a reduced solubility compared with a near-ideal gas, thereby producing negative deviations from predicted partition coefficients. All of the deviation trends are suitably described using a second order polynomial fit for CO_2 densities up to 656 kg/m^3. This fit provides a means to correct the existing pure noble gas–water partition coefficients derived from pure noble gas/water systems for use within high density CO_2 systems.

ACKNOWLEDGEMENTS

This research was supported by grants NE/F002823/1 and NE/F002645/1 from the UK Natural Environment Research Council as part of the CRIUS consortium, which included a PhD studentship to O.W. Thanks are given to John Cowpe, Bevist Clementson, Dave Blagburn and Cath Davies for extensive assistance within the laboratory in Manchester, and to Gemma Purser and Keith Bateman for assistance with the high-pressure system at the BGS. C.R. published with the permission of the Executive Director of the British Geological Survey, NERC. Reviews from Daniele Pinti and two anonymous reviewers greatly improved the manuscript.

APPENDIX 1. CALCULATING MEASUREMENT UNCERTAINTIES

Uncertainty was assessed using a two-tiered approach. Firstly all relative measurement uncertainties for each isotopic Henry's constant were combined via addition in quadrature. All measurement uncertainties are described in Table A1 and the detailed methodology for calculating this uncertainty is given in this appendix.

However not all sources of uncertainty (e.g., the accuracy of NIST-derived densities) were satisfactorily included within this measurement uncertainty. All remaining sources of uncertainty would therefore affect reproducibility of each paired sample. Consequently, by determining the reproducibility uncertainty ($\Delta\overline{D}_{\mathrm{Proc}(P,T)}$), all additional uncertainties could be reasonably incorporated. The process of deriving the reproducibility uncertainty for each isotope and combining it with the measurement uncertainty is outlined in this appendix.

To generate overall uncertainty for noble gases where multiple isotopes were analysed, arithmetic means were taken of each overall uncertainty and were divided by $\sqrt{n}$ where n is the number of isotopes being combined.

Calculating measurement uncertainties

Experimental and sampling densities for the density correction were calculated using the respective pressures and temperatures via the NIST website (NIST, 2014). Therefore the corresponding uncertainty was considered a function of each of these values. Thus these were added

Table A1
Measurement uncertainties for generating a partition coefficient for each isotope from a paired analysis. Pressure and temperature uncertainties are taken from the ESI Technology transducer manual and the Isotech calibration unit temperature probe manual respectively.

Uncertainty factor	Symbol	Calculated uncertainty	Units
Noble gas isotope i in CO_2 phase	$\Delta C_{i(P,T)}$	1σ of average peak intensity	bar
Noble gas isotope i in H_2O phase	$\Delta W_{i(P,T)}$	1σ of average peak intensity	bar
Volume of CO_2 sampler	ΔC_A	1 S.E. of mean volume	cm^3
Volume of H_2O sampler	ΔW_A	1 S.E. of mean volume	cm^3
Aliquot correction factor	ΔF	0.1275 (1 S.E. of mean)	N/A
Density correction for CO_2 phase	$\Delta\rho_C$	Measurement uncertainty in pressure and temperature	kg/m^3
Density correction for H_2O phase	$\Delta\rho_W$	Measurement uncertainty in pressure and temperature	kg/m^3
Uncertainty in pressure	ΔP	1	bar
Uncertainty in temperature	ΔT	0.2	°C

in quadrature to calculate the relative uncertainty from the density correction:

$$\frac{\Delta\rho_A}{\rho_A} = \sqrt{\left(\frac{\Delta T_{\text{Samp}}}{T_{\text{Samp}}}\right)^2 + \left(\frac{\Delta P_{\text{Samp}}}{P_{\text{Samp}}}\right)^2 + \left(\frac{\Delta T_{\text{Exp}}}{T_{\text{Exp}}}\right)^2 + \left(\frac{\Delta P_{\text{Exp}}}{P_{\text{Exp}}}\right)^2} \quad \text{(A1)}$$

where ρ_A is the density correction factor for phase A, T_{Samp} and P_{Samp} are sampling temperatures and pressures, T_{Exp} and P_{Exp} are experimental temperatures and pressures and Δ denotes the corresponding uncertainty.

To calculate the net relative uncertainty for each partition coefficient calculated from a paired set of samples these relative uncertainties were added in quadrature:

$$\frac{\Delta D_{i(P,T)}}{D_{i(P,T)}} = \sqrt{\left(\frac{\Delta C_{i(P,T)}}{C_{i(P,T)}}\right)^2 + \left(\frac{\Delta W_{i(P,T)}}{W_{i(P,T)}}\right)^2 + \left(\frac{\Delta C_V}{C_V}\right)^2 + \left(\frac{\Delta W_V}{W_V}\right)^2 + \left(\frac{\Delta F_i}{F_i}\right)^2 + \left(\frac{\Delta \rho_C}{\rho_C}\right)^2 + \left(\frac{\Delta \rho_W}{\rho_W}\right)^2} \quad \text{(A2)}$$

By multiplying this relative uncertainty by the partition coefficient the absolute uncertainty could be determined. Thus uncertainty for each partition coefficient was derived for a CO_2–water paired set of samples.

To combine the paired samples for each noble gas at a given density each relative uncertainty was added in quadrature. These were then divided by the number of paired samples used for creating this average ($n_{(\text{P,T})}$). This was then square-rooted to give the average relative uncertainty for a given density:

$$\frac{\Delta \overline{D}_{i\text{Exp}(P,T)}}{\overline{D}_{i\text{Exp}(P,T)}} = \sqrt{\frac{\sum_1^n \left(\frac{\Delta D_{i(P,T)}}{D_{i(P,T)}}\right)^2}{(n_{(P,T)})}} \quad \text{(A3)}$$

Assessing the reproducibility uncertainty

This was calculated using the average deviation of partition coefficients from the mean values. For this, each partition coefficient for a given isotope i ($D_{i(P,T)}$) was subtracted from the mean ($\bar{D}_{i(P,T)}$) to give the absolute deviation. By dividing each deviation by the mean value a relative deviation of each individual data point from the mean was calculated. These relative uncertainties for every partition coefficient were then all added in quadrature and divided by the total number of samples (n_{tot}). Finally this was square-rooted to generate the average the relative procedural reproducibility uncertainty for each isotope:

$$\frac{\Delta \overline{D}_{i\text{Proc}}}{\overline{D}_{i\text{Proc}}} = \sqrt{\frac{\sum_1^{n_{\text{tot}}} \left(\frac{\left(\left|\overline{D}_{i(P,T)} - D_{i(P,T)}\right|\right)}{\overline{D}_{i(P,T)}}\right)^2}{n_{\text{tot}}}} \quad \text{(A4)}$$

This uncertainty could then be added in quadrature with the experimental uncertainty to yield the overall uncertainty for isotope i at a given density:

$$\frac{\Delta \overline{D}_{i(P,T)}}{\overline{D}_{i(P,T)}} = \sqrt{\left(\frac{\Delta \overline{D}_{i\text{Exp}(P,T)}}{\overline{D}_{i\text{Exp}(P,T)}}\right)^2 + \left(\frac{\Delta \overline{D}_{i\text{Proc}}}{\overline{D}_{i\text{Proc}}}\right)^2} \quad \text{(A5)}$$

APPENDIX 2. SYSTEM STABILITY AND LINEARITY

System stability

System stability was evaluated by measuring the ^{40}Ar content of six independent 0.2264 cm^3 air calibrations over the course of a day. The mean and standard error was compared with 4 identical measurements collected 6 months previously. The mean and standard error are shown in Table A2 and demonstrate sufficient system stability for quantitative analysis.

Table A2
Assessment of system stability using air calibrations. The average ^{40}Ar content of six single 0.2264 cm^3 air calibrations taken over a day are compared with four single 0.2264 cm^3 calibrations analysed over the course of a day 6 months prior. Percentage change is the increase in average values over this period. Uncertainty is quoted as one standard error.

6 ^{40}Ar air calibrations (bar)	4 ^{40}Ar air calibrations 6 months prior (bar)	Percentage change (%)	Combined ^{40}Ar values (bar)
9.37 ($\pm$0.09) $\times$ 10^{-11}	9.58 ($\pm$0.10) $\times$ 10^{-11}	2.23 ($\pm$1.45)	9.45 ($\pm$0.09) $\times$ 10^{-11}

Table A3
Assessment of signal intensity calibration. The average signal response at mass 40 (^{40}Ar) of six single 0.2264 cm^3 air standards compared to the average ^{40}Ar content of three 4 $\times$ 0.2264 cm^3 air standards. Deviation from linearity was calculated as the percentage by which measured four-shot values differed from the expected values. Uncertainty is quoted as one standard error.

^{40}Ar in 1 $\times$ air standard (bar)	Expected ^{40}Ar in 4 $\times$ air standard (bar)	Measured ^{40}Ar in 4 $\times$ air standard (bar)	Deviation from linearity (%)
6.67 ($\pm$0.10) $\times$ 10^{-11}	2.67 ($\pm$0.04) $\times$ 10^{-10}	2.73 ($\pm$0.16) $\times$ 10^{-10}	2.2 ($\pm$6.3)

System linearity

At higher pressures, ionisation and signal response in quadrupole mass spectrometers can become non-linear. This was assessed for the system using 0.2264 cm^3 aliquots of air standards, corrected for temperature, pressure, altitude and humidity. Single aliquots were analysed for ^{40}Ar, the noble gas with the highest partial pressure. These were compared with quadruple (i.e., $4 \times$ single 0.2264 cm^3) air standards. The range present fully covers the maximum range of operational pressures within the experimental program. The results are presented in Table 12 and confirms the linearity of the system within uncertainty for argon. Linearity for all other noble gases was assessed using the noble gas spike which had been diluted and expanded into known volumes (Ampule and aliquot A1) on the analytical line (Fig. 3). The relative signal intensities were compared for all noble gases and all were found to produce a linear response across the experimental range comparable to argon which was also measured as a control.

REFERENCES

Aubry G., Sator N. and Guillot B. (2013) Vesicularity, bubble formation and noble gas fractionation during MORB degassing. *Chem. Geol.* **343**, 85–98.

Bachu S. (2003) Screening and ranking of sedimentary basins for sequestration of CO_2 in geological media in response to climate change. *Environ. Geol.* **44**, 277–289.

Baiker A. (1999) Supercritical fluids in heterogeneous catalysis. *Chem. Rev.* **99**, 453–473.

Ballentine C. J. and Holland G. (2008) What CO_2 well gases tell us about the origin of noble gases in the mantle and their relationship to the atmosphere. *Philos. Trans. R. Soc. A Math. Phys. Eng. Sci.* **366**, 4183–4203.

Ballentine C. J., Schoell M., Coleman D. and Cain B. A. (2001) 300 Myr old magmatic CO_2 in natural gas reservoirs of the West Texas Permian basin. *Nature* **409**, 327–331.

Ballentine C. J., Burgess R. and Marty B. (2002) Tracing fluid origin, transport and interaction in the crust. In *Noble Gases in Geochemistry and Cosmochemistry. Reviews in Mineralogy and Geochemistry* (eds. D. Porcelli, C. J. Ballentine and R. Wieler). Mineralogical Society of America, pp. 539–614.

Bickle M., Chadwick A., Huppert H. E., Hallworth M. and Lyle S. (2007) Modelling carbon dioxide accumulation at Sleipner: implications for underground carbon storage. *Earth Planet. Sci. Lett.* **255**, 164–176.

Biggerstaff D. R. and Wood R. H. (1988) Apparent molar volumes of aqueous argon, ethylene, and xenon from 300 K to 716 K. *J. Phys. Chem.* **92**, 1988–1994.

Black H. (1996) Supercritical carbon dioxide: the "greener" solvent. *Environ. Sci. Technol.* **30**, A124–A127.

Blunt M., Fayers F. J. and Orr F. M. (1993) Carbon dioxide in enhanced oil recovery. *Energy Convers. Manage.* **34**, 1197–1204.

Brennwald M. S., Vogel N., Scheidegger Y., Tomonaga Y., Livingstone D. M. and Kipfer R. (2013) Noble gases as environmental tracers in sediment porewaters and in stalagmite fluid inclusions. In *The Noble Gases as Geochemical Tracers* (ed. P. Burnard). Springer, pp. 123–154.

Briones J. A., Mullins J. C., Thies M. C. and Kim B. U. (1987) Ternary phase-equilibria for acetic acid–water mixtures with supercritical carbon-dioxide. *Fluid Phase Equilib.* **36**, 235–246.

Burnard P. (2013) *The Noble Gases as Geochemical Tracers*. Springer, Berlin Heidelberg.

Carroll M. R. and Draper D. S. (1994) Noble gases as trace elements in magmatic processes. *Chem. Geol.* **117**, 37–56.

Cole D. R., Chialvo A. A., Rother G., Vlcek L. and Cummings P. T. (2010) Supercritical fluid behavior at nanoscale interfaces: implications for CO_2 sequestration in geologic formations. *Philos. Mag.* **90**, 2339–2363.

Crovetto R., Fernandez-Prini R. and Japas M. L. (1982) Solubilities of inert gases and methane in H_2O and in D_2O in the temperature range of 300 to 600 K. *J. Chem. Phys.* **76**, 1077–1088.

Diamond L. W. and Akinfiev N. N. (2003) Solubility of CO_2 in water from −1.5 to 100 °C and from 0.1 to 100 MPa: evaluation of literature data and thermodynamic modelling. *Fluid Phase Equilib.* **208**, 265–290.

Dubacq B., Bickle M. J., Wigley M., Kampman N., Ballentine C. J. and Lollar B. S. (2012) Noble gas and carbon isotopic evidence for CO_2-driven silicate dissolution in a recent natural CO_2 field. *Earth Planet. Sci. Lett.* **341**, 10–19.

Enns T., Scholand P. F. and Bradstre E. D. (1965) Effect of hydrostatic pressure on gases dissolved in water. *J. Phys. Chem.* **69**, 389–391.

Ferrieri R. A. (2003) Supercritical fluids in medical radioisotope processing and chemistry, Part II: applications – real and demonstrated. *J. Labelled Compd. Radiopharm.* **46**, 923–943.

Friedmann S. J. (2007) Geological carbon dioxide sequestration. *Elements* **3**, 179–184.

Gerth W. A. (1983) Effects of dissolved electrolytes on the solubility and partial molar volume of helium in water from 50 to 400 atmospheres at 25 °C. *J. Solution Chem.* **12**, 655–669.

Giddings J. C., Myers M. N., Mclaren L. and Keller R. A. (1968) High pressure gas chromatography of non-volatile species. *Science* **162**, 67–73.

Gilfillan S. M., Ballentine C. J., Holland G., Blagburn D., Lollar B. S., Stevens S., Schoell M. and Cassidy M. (2008) The noble gas geochemistry of natural CO_2 gas reservoirs from the Colorado Plateau and Rocky Mountain provinces, USA. *Geochim. Cosmochim. Acta* **72**, 1174–1198.

Gilfillan S. M. V., Lollar B. S., Holland G., Blagburn D., Stevens S., Schoell M., Cassidy M., Ding Z. J., Zhou Z., Lacrampe-Couloume G. and Ballentine C. J. (2009) Solubility trapping in formation water as dominant CO_2 sink in natural gas fields. *Nature* **458**, 614–618.

Guillot B. and Sarda P. (2006) The effect of compression on noble gas solubility in silicate melts and consequences for degassing at mid-ocean ridges. *Geochim. Cosmochim. Acta* **70**, 1215–1230.

Halliday A. N. (2013) The origins of volatiles in the terrestrial planets. *Geochim. Cosmochim. Acta* **105**, 146–171.

Hilton D. R. and Porcelli D. (2003) Noble gases as mantle tracers. In *Treatise on Geochemistry* (eds. R. W. Carlson, H. Holland and K. Turekian). Elsevier, pp. 277–318.

Holland G., Cassidy M. and Ballentine C. J. (2009) Meteorite Kr in Earth's mantle suggests a late accretionary source for the atmosphere. *Science* **326**, 1522–1525.

Hou S. X., Maitland G. C. and Trusler J. P. M. (2013) Measurement and modeling of the phase behavior of the (carbon dioxide plus water) mixture at temperatures from 298.15 K to 448.15 K. *J. Supercrit. Fluids* **73**, 87–96.

Hunt A. G., Darrah T. H. and Poreda R. J. (2012) Determining the source and genetic fingerprint of natural gases using noble gas geochemistry: a northern Appalachian Basin case study. *AAPG Bull.* **96**, 1785–1811.

IPCC (2005) *Carbon Dioxide Capture and Storage*. Cambridge University Press.

Jambon A., Weber H. and Braun O. (1986) Solubility of He, Ne, Ar, Kr and Xe in a basalt melt in the range 1250–1600 °C. Geochemical implications. *Geochim. Cosmochim. Acta* **50**, 401–408.

Kamihira M., Taniguchi M. and Kobayashi T. (1987) Removal of organic solvent from antibiotics with supercritical carbon dioxide. *J. Ferment. Technol.* **65**, 71–75.

Kampman N., Maskell A., Bickle M. J., Evans J. P., Schaller M., Purser G., Zhou Z., Gattacceca J., Peitre E. S., Rochelle C. A., Ballentine C. J. and Busch A. (2013) Scientific drilling and downhole fluid sampling of a natural CO_2 reservoir, Green River, Utah. *Sci. Dril.* **16**, 33–43.

Kauffman J. F. (2001) Quadrupolar solvent effects on solvation and reactivity of solutes dissolved in supercritical CO_2. *J. Phys. Chem. A* **105**, 3433–3442.

Kharaka Y. K., Cole D. R., Hovorka S. D., Gunter W. D., Knauss K. G. and Freifeld B. M. (2006) Gas–water–rock interactions in Frio Formation following CO_2 injection: implications for the storage of greenhouse gases in sedimentary basins. *Geology* **34**, 577–580.

Kim W. J., Kim J. D., Kim J., Oh S. G. and Lee Y. W. (2008) Selective caffeine removal from green tea using supercritical carbon dioxide extraction. *J. Food Eng.* **89**, 303–309.

Kipfer R., Aeschbach-Hertig W., Peeters F. and Stute M. (2002) Noble gases in lakes and ground waters. In *Noble Gases in Geochemistry and Cosmochemistry. Reviews in Mineralogy and Geochemistry* (eds. D. Porcelli, C. J. Ballentine and R. Wieler). Mineralogical Society of America, pp. 615–700.

Mackintosh S. J. and Ballentine C. J. (2012) Using $^3He/^4He$ isotope ratios to identify the source of deep reservoir contributions to shallow fluids and soil gas. *Chem. Geol.* **304**, 142–150.

Marty B. (2012) The origins and concentrations of water, carbon, nitrogen and noble gases on Earth. *Earth Planet. Sci. Lett.* **313**, 56–66.

Mohamed R. S., Saldana M. D. A., Mazzafera P., Zetzl C. and Brunner G. (2002) Extraction of caffeine, theobromine, and cocoa butter from Brazilian cocoa beans using supercritical CO_2 and ethane. *Ind. Eng. Chem. Res.* **41**, 6751–6758.

Moore J. C., Battino R., Rettich T. R., Handa Y. P. and Wilhelm E. (1982) Partial molar volumes of gases at infinite dilution in water at 298.15-K. *J. Chem. Eng. Data* **27**, 22–24.

Morgenstern D. A., LeLacheur R. M., Morita D. K., Borkowsky S. L., Feng S., Brown G. H., Luan L., Gross M. F., Burk M. J. and Tumas W. (1996) Supercritical carbon dioxide as a substitute solvent for chemical synthesis and catalysis. *Green Chem.* **626**, 132–151.

Nimz G. J. and Hudson G. B. (2005) The use of noble gas isotopes for monitoring leakage of geologically stored CO_2. In *Carbon Dioxide Capture for Storage in Deep Geologic Formations* (eds. D. Thomas and S. Benson). Elsevier Press, pp. 1113–1130.

NIST. 2014. *Thermophysical Properties of Fluid Systems*, <http://webbook.nist.gov/chemistry/fluid/>.

Paonita A. and Martelli M. (2006) Magma dynamics at mid-ocean ridges by noble gas kinetic fractionation: assessment of magmatic ascent rates. *Earth Planet. Sci. Lett.* **241**, 138–158.

Paonita A. and Martelli M. (2007) A new view of the He–Ar–CO_2 degassing at mid-ocean ridges: homogeneous composition of magmas from the upper mantle. *Geochim. Cosmochim. Acta* **71**, 1747–1763.

Pinti D. L., Castro M. C., Shouakar-Stash O., Tremblay A., Garduno V. H., Hall C. M., Helie J. F. and Ghaleb B. (2013) Evolution of the geothermal fluids at Los Azufres, Mexico, as traced by noble gas isotopes, $\delta^{18}O$, δD, $\delta^{13}C$ and $^{87}Sr/^{86}Sr$. *J. Volcanol. Geoth. Res.* **249**, 1–11.

Poling B. E., Prausnitz J. M., O'Connell J. P. and Knovel (2001) *The Properties of Gases and Liquids*, fifth ed. McGraw-Hill, New York.

Porcelli D., Ballentine C. J. and Wieler R. (2002) An overview of noble gas geochemistry and cosmochemistry. In *Noble Gases in Geochemistry and Cosmochemistry. Reviews in Mineralogy and Geochemistry* (eds. D. Porcelli, C. J. Ballentine and R. Wieler). Mineralogical Society of America, pp. 1–18.

Prini R. F. and Crovetto R. (1989) Evaluation of data on solubility of simple apolar gases in light and heavy-water at high-temperature. *J. Phys. Chem. Ref. Data* **18**, 1231–1243.

Ravagnani A. T. F. S. G., Ligero E. L. and Suslick S. B. (2009) CO_2 sequestration through enhanced oil recovery in a mature oil field. *J. Petrol. Sci. Eng.* **65**, 129–138.

Raveendran P., Ikushima Y. and Wallen S. L. (2005) Polar attributes of supercritical carbon dioxide. *Acc. Chem. Res.* **38**, 478–485.

Reverchon E., Adami R., Cardea S. and Della Porta G. (2009) Supercritical fluids processing of polymers for pharmaceutical and medical applications. *J. Supercrit. Fluids* **47**, 484–492.

Reynolds L., Gardecki J. A., Frankland S. J. V., Horng M. L. and Maroncelli M. (1996) Dipole solvation in nondipolar solvents: experimental studies of reorganization energies and solvation dynamics. *J. Phys. Chem.* **100**, 10337–10354.

Sarda P. and Guillot B. (2005) Breaking of Henry's law for noble gas and CO_2 solubility in silicate melt under pressure. *Nature* **436**, 95–98.

Sherwood-Lollar B. and Ballentine C. J. (2009) Insights into deep carbon derived from noble gases. *Nat. Geosci.* **2**, 543–547.

Smith S. P. (1985) Noble gas solubility in water at high temperature. *Trans. Am. Geophys. Union* **66**, 397-397.

Smith S. P. and Kennedy B. M. (1983) The solubility of noble gases in water and in NaCl brine. *Geochim. Cosmochim. Acta* **47**, 503–515.

Span R. and Wagner W. (1996) A new equation of state for carbon dioxide covering the fluid region from the triple-point temperature to 1100 K at pressures up to 800 MPa. *J. Phys. Chem. Ref. Data* **25**, 1509–1596.

Sparks R. S. J. (1978) The dynamics of bubble formation and growth in magmas: a review and analysis. *J. Volcanol. Geoth. Res.* **3**, 1–37.

Spycher N., Pruess K. and Ennis-King J. (2003) CO_2–H_2O mixtures in the geological sequestration of CO_2 I. Assessment and calculation of mutual solubilities from 12 to 100 °C and up to 600 bar. *Geochim. Cosmochim. Acta* **67**, 3015–3031.

Warr O. (2013) *Understanding Phase Behavior in the Geological Storage of Carbon Dioxide*. University of Manchester, Manchester, <https://www.escholar.manchester.ac.uk/uk-ac-man-scw:214069>.

Yonker C. R., Frye S. L., Kalkwarf D. R. and Smith R. D. (1986) Characterization of supercritical fluid solvents using solvatochromic shifts. *J. Phys. Chem.* **90**, 3022–3026.

Zhou Z., Ballentine C. J., Kipfer R., Schoell M. and Thibodeaux S. (2005) Noble gas tracing of groundwater/coalbed methane interaction in the San Juan Basin, USA. *Geochim. Cosmochim. Acta* **69**, 5413–5428.

Zhou Z., Ballentine C. J., Schoell M. and Stevens S. H. (2012) Identifying and quantifying natural CO_2 sequestration processes over geological timescales: the Jackson Dome CO_2 Deposit, USA. *Geochim. Cosmochim. Acta* **86**, 257–275.

Associate editor: Chris M. Hall